

# Atrous Convolutional Neural Network (ACNN) for Semantic Image Segmentation with full-scale Feature Maps

Xiao-Yun Zhou, *Student Member, IEEE*, Jian-Qing Zheng, Guang-Zhong Yang, *Fellow, IEEE*

arXiv:1901.09203v2 [cs.LG] 10 Feb 2019

**Abstract**—Deep Convolutional Neural Networks (DCNNs) are used extensively in biomedical image segmentation. However, current DCNNs usually use down sampling layers for increasing the receptive field and gaining abstract semantic information. These down sampling layers decrease the spatial dimension of feature maps, which can be detrimental to semantic image segmentation. Atrous convolution is an alternative for the down sampling layer. It increases the receptive field whilst maintains the spatial dimension of feature maps. In this paper, a method for effective atrous rate setting is proposed to achieve the largest and fully-covered receptive field with a minimum number of atrous convolutional layers. Furthermore, different atrous blocks, shortcut connections and normalization methods are explored to select the optimal network structure setting. These lead to a new and full-scale DCNN - Atrous Convolutional Neural Network (ACNN), which incorporates cascaded atrous ll-blocks, residual learning and Fine Group Normalization (FGN). Application results of the proposed ACNN to Magnetic Resonance Imaging (MRI) and Computed Tomography (CT) image segmentation demonstrate that the proposed ACNN can achieve comparable segmentation Dice Similarity Coefficients (DSCs) to U-Net, optimized U-Net and hybrid network, but with significantly reduced trainable parameters due to the use of full-scale feature maps and therefore computationally is much more efficient for both the training and inference.

**Index Terms**—Deep Convolutional Neural Network (DCNN), Atrous Convolutional Neural Network (ACNN), semantic image segmentation, full-scale feature maps.

## I. INTRODUCTION

**B**IOMEDICAL semantic image segmentation which predicts the class, anatomy, or prosthesis of each pixel in an image is important for a wide range of applications. "Semantic" is used to distinguish between instance segmentation which predicts the instance of a pixel as well. Conventional methods are based on ad hoc, expert-designed feature extractors and classifiers. Recently, the use of Deep Convolutional Neural Networks (DCNNs) has shown promising results for many vision-based tasks including image classification [1], object detection [2], and semantic image segmentation [3]. In DCNN, features are extracted and classified automatically by training multiple non-linear modules [4]. Unlike traditional fully-connected neural networks where each output node is linked to all input nodes, an output node of DCNN only links to regional input nodes, known as the receptive field (the input nodes that an output node sees). Multiple convolutional layers, as shown in Fig. 1a, and down sampling layers, i.e., pooling layers shown in Fig. 1b, are cascaded to achieve a large receptive field coverage. This large receptive field is essential for extracting and classifying underlying visual features and semantic details. The use of this kind of DCNN means that the feature map is also down sampled, which can be detrimental to pixel-level tasks, i.e., segmentation. For

biomedical images with focal lesions, local features with small sizes may be discarded due to down sampling.

In order to compensate for decreased dimension of feature maps, various techniques have been proposed. For example, deconvolutional layers and non-linear up-sampling are used respectively in Fully Convolutional Neural Network (FCNN) [5] and SegNet [6] to recover the down-sampled feature map to the input image size. An alternative is to use atrous convolution [3], also known as dilated convolution [7], to replace the down sampling layer in traditional DCNNs to increase the receptive field. Atrous convolution inserts zeros between non-zero filter taps to sample the feature map as shown in Fig. 1c. It increases the receptive field with the atrous rate but maintains the spatial dimension of feature maps without increasing the computational complexity. However, applying atrous convolution introduces a high demand on memory usage and the inserted zeros of atrous convolution cause input node or information missing. These challenges have limited the practical use of atrous convolution, particularly for biomedical semantic image segmentation.

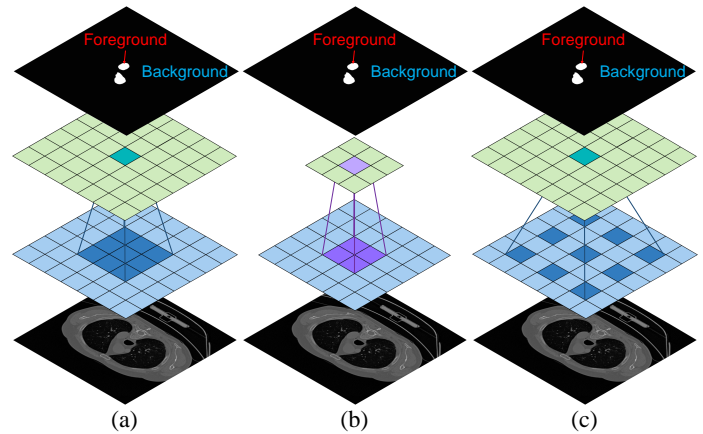


Fig. 1. Illustrations of using DCNN with different receptive fields for biomedical semantic image segmentation: (a) convolutional layer with a  $3 \times 3$  receptive field; (b) pooling layer with a  $2 \times 2$  receptive field; (c) atrous convolutional layer (atrous rate is 2) with a  $5 \times 5$  receptive field.

As mentioned above, memory shortage is the first challenge for applying atrous convolution, as high-resolution feature map propagation consumes a large amount of memory. In previous work, atrous convolution was usually applied jointly with down sampling layers as a trade-off between the accuracy and memory. For example, in Deeplab [3], a feature map at  $1/8$  spatial size of the input image was first extracted by multiple convolutional and down sampling layers. Feature maps with a larger receptive field but with the same  $1/8$  spatial size were then calculated by multiple atrous convolutional layers. Subsequently, bilinear interpolation was used to recover the spatial dimension of the down-sampled feature maps, while conditional random field was used to refine the predicted pixel-level probability. In multi-scale context aggregation [7], a feature map with  $64 \times 64$  dimension was firstly down-sampled from the input image, then a context module with seven atrous convolutional layers was applied to extract features with a larger receptive field at the same spatial

Manuscript received \*\* \*\*, 2019; This work was supported by Engineering and Physical Sciences Research Council (EPSRC) project grant EP/L020688/1.

Xiao-Yun Zhou(e-mail: xiaoyun.zhou14@imperial.ac.uk), Jian-Qing Zheng and Guang-Zhong Yang are with the Hamlyn Centre for Robotic Surgery, Imperial College London, UK.

This work has been submitted to the IEEE for possible publication. Copyright may be transferred without notice, after which this version may no longer be accessible.

dimension. Similar joint usage of atrous convolutional and down sampling layers can also be found in [8].

In practice, setting the atrous rates is another challenge when applying atrous convolution. This is because the output node only links to input nodes which align with non-zero filter taps, as shown in Fig. 1c. The input nodes which align with zero filter taps are not considered. There are thus far no standard ways of setting the atrous rates. For example, an atrous rate setting of (1, 1, 2, 4, 8, 16, 1) was allocated for achieving a receptive field of  $67 \times 67$  in [7] following the strides of max-pooling layers in FCNN. Wang et al. found that an atrous rate setting of (2, 4, 8) would cause gridding effects (regular input nodes are missed) and proposed a hybrid atrous rate setting, i.e., (1, 2, 5, 9) to guarantee coverage of all input nodes [8]. An atrous rate setting of (6, 12, 18) was used for each block and an atrous rate setting of (1, 2, 4) was set inside each block in [9] based on empirical knowledge.

In this paper, we propose a full-scale DCNN where the spatial dimension of intermediate feature maps remains the same as that of the input image. This is different from the work of [10], for which the spatial dimension of intermediate feature maps at the residual stream is still smaller than that of the input image. For proposing a full-scale DCNN, the proposed network needs to: 1) maximize the receptive field with as few atrous convolutional layers as possible to save memory usage; 2) fully cover the receptive field without missing any input node. In the following sections, we first prove a method that sets the atrous rate as  $(k)^{n-1}$  at the  $n^{\text{th}}$  atrous convolutional layer, where  $k$  is the kernel size and  $n$  is the sequence number of atrous convolutional layer, can achieve the largest and fully-covered receptive field with a minimum number of atrous convolutional layers in Sec. II-A. Then six atrous blocks, three shortcut connections and four different normalization methods are explored in Sec. II-B.1, Sec. II-B.2 and Sec. II-B.3, respectively, to select the optimal atrous block, shortcut connection and normalization method through experimental investigations. Finally, a full-scale DCNN - Atrous Convolutional Neural Network (ACNN) is proposed by using multiple cascaded atrous II-blocks, residual learning and Fine Group Normalization (FGN) in Sec. II-B.4. Cardiovascular Magnetic Resonance Imaging (MRI) and Computed Tomography (CT) image segmentation of the Right Ventricle (RV), Left Ventricle (LV) and aorta are used to validate the proposed ACNN with data collection shown in Sec. II-C and with results shown in Sec. III. U-Net [11], optimized U-Net [12] and a hybrid network similar to [3] are used as the comparison for performance assessment. It has been shown that the proposed ACNN can achieve comparable segmentation Dice Similarity Coefficients (DSCs) compared to other techniques with much less trainable parameters and model sizes, indicating the benefit of full-scale feature maps in DCNN. Discussions and conclusions are stated in Sec. IV and Sec. V respectively.

## II. METHODOLOGY

### A. Atrous Rate Setting

In this section, we focus on optimizing the atrous rate setting which would achieve the largest and fully-covered receptive field with a minimum number of atrous convolutional layers. Before presenting the detailed mathematical derivation, three 1D receptive field examples with three different atrous rate settings are intuitively shown in Fig. 2. In this three-layer network, with an atrous rate setting of (1, 2, 4), a receptive field of 15 is achieved, while with an atrous rate setting of (1, 2, 9), a receptive field of 25 is achieved with a coverage ratio (the ratio of linked input nodes over all input nodes in the receptive field) of 0.84. With the proposed atrous rate setting of (1, 3, 9), the largest receptive field of 27 is achieved with a full coverage, i.e.,

the coverage ratio is 1.0. Detailed mathematical proofs are presented below. For simplification, batch size is considered as 1 here.

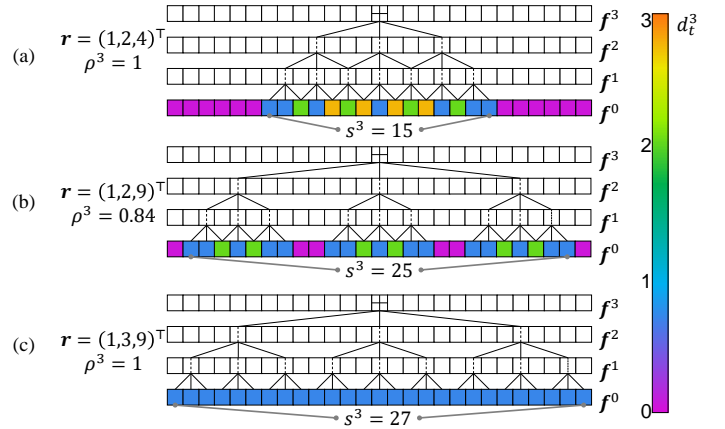


Fig. 2. Three 1D receptive field examples with different atrous rate settings for a three-layer network: (a) an atrous rate setting of (1, 2, 4), (b) an atrous rate setting of (1, 2, 9), (c) an atrous rate setting of (1, 3, 9). The colour represents the link number from the bottom/input node to the top central/output node.  $\rho^3$  is the coverage ratio defined by (7),  $\mathbf{r}$  is the atrous rate array,  $s^3$  is the receptive field size,  $\mathbf{f}^{(1 \sim 3)}$  is the 1D feature map,  $\mathbf{f}^0$  is the 1D input image,  $d_t^3$  is the receptive field of  $\mathbf{f}_0^0$ , these notations are explained and used in Sec. II-A.

With an input feature map  $\mathbf{F}^{n-1}$  of size  $H \times W \times c_{n-1}$ , an output feature map  $\mathbf{F}^n$  of size  $H \times W \times c_n$  is calculated by the  $n^{\text{th}}$  atrous convolutional layer with an atrous rate  $r_n$ , where  $\mathbf{F}^0 \in \mathbb{R}^{H \times W \times c_0}$ ,  $\mathbf{F}^n \in \mathbb{R}^{H \times W \times c_n}$ ,  $n \in [1, N] \cap \mathbb{N}$ , and  $\mathbf{r} = (r_1 \cdots r_N)^T \in \mathbb{N}^N$ , where  $N \in \mathbb{Z}_+$  is the total number of atrous convolutional layers. Here  $H \in \mathbb{N}$  is the feature height and  $W \in \mathbb{N}$  is the feature width, though these two values are usually equal for medical images. The channel number of feature maps is denoted as  $\mathbf{c} = (c_0 \cdots c_N)^T \in \mathbb{N}^{N+1}$ , and  $\mathbf{F}^0$  is the input image. By ignoring the non-linear modules, i.e., relu, and the biases, an equivalent 2D atrous convolution could achieve a backward propagation from  $\mathbf{F}^n$  to  $\mathbf{F}^{n-1}$ , which can be decomposed into two 1D atrous convolutions [13], with kernel  $\mathbf{v}^n$  indexed by  $t \in \mathbb{Z}$ :

$$v_t^n(k, r_n) = \sum_{u=-\frac{k-1}{2}}^{\frac{k-1}{2}} w_u^n \cdot \delta(t - ur_n), \text{ where } \delta(t) := \begin{cases} 1 & t = 0 \\ 0 & t \neq 0 \end{cases} \quad (1)$$

Here,  $k$  is an odd number which represents the kernel size, i.e., 3, 5, or 7.  $t$  is the pixel index.  $w_u^n$ , each element of weight matrix  $\mathbf{w}^n \in \mathbb{R}^k$ , is a trainable variable.  $\mathbf{1}(t) : \mathbb{Z} \rightarrow \{0, 1\}$  is an indicator function defined as:

$$\mathbf{1}(t) := \begin{cases} 1 & t = 0 \\ 0 & t \neq 0 \end{cases} \quad (2)$$

Denote vectors  $\mathbf{f}^0, \mathbf{f}^n$  as the 1D input image and the  $n^{\text{th}}$  1D feature map, both indexed by  $t$ .  $\mathbf{f}^0$  can be calculated from  $\mathbf{f}^n$  by:

$$\mathbf{f}^0 = \mathbf{v}^1 * \cdots * \mathbf{v}^n * \mathbf{f}^n \quad (3)$$

Define  $\mathbf{d}^n(k, \mathbf{r}) := \mathbf{f}^0(\mathbf{f}^n = \mathbf{1}(t))$ , in which  $\mathbf{f}^n = \mathbf{1}(t)$  indicates that only the central pixel of  $\mathbf{f}^n$  is with a non-zero value (=1). It is calculated as:

$$\mathbf{d}^n(k, \mathbf{r}) := \mathbf{v}^1 * \cdots * \mathbf{v}^n * \delta(t) \quad (4)$$

By setting  $\mathbf{w}^n = (1)_k, \forall n$ , vectors consisting of 1, then  $d_t^n \in \mathbb{N}$ , the element indexed by  $t \in \mathbb{Z}$ , is the link number from  $\mathbf{f}_0^0$  to the input image's pixel or node. Thus,  $\mathbf{d}^n$  represents the receptive field

of  $f_0^n$ , where its receptive field coverage could be represented by the non-zero element number in vector  $\mathbf{d}^n$ :

$$\|\mathbf{d}^n\|_0 := \sum_t (1 - \mathbf{1}(d_t^n)) \quad (5)$$

and its receptive field size  $s^n \in \mathbb{N}$  is calculated as:

$$s^n(k, \mathbf{r}) = 1 + (k-1) \sum_{m=1}^n r_m \quad (6)$$

The receptive field coverage ratio of  $f_0^n$ , denoted by  $\rho^n \in \mathbb{R}_+$ , is then defined as:

$$\rho^n(k, \mathbf{r}) := \frac{\|\mathbf{d}^n\|_0}{s^n} \quad (7)$$

In order to ensure a fully-covered receptive field from an output pixel or node, our target is to maximize the receptive field size with a constraint of receptive field coverage ratio:

$$\max_{\mathbf{r} \in \mathbb{N}^N} \left\{ s^N : \rho^N = 1 \right\} \quad (8)$$

By substituting (6) and (7) into (8), the optimization problem can be converted as:

$$\max_{\mathbf{r} \in \mathbb{N}^N} \left\{ \|\mathbf{d}^N\|_0 : \|\mathbf{d}^N\|_0 = 1 + (k-1) \sum_{n=1}^N r_n \right\} \quad (9)$$

The total link number from  $f_0^n$  to  $f^0$  is represented by:

$$\|\mathbf{d}^n\|_1 = \sum_t d_t^n = (k)^n \quad (10)$$

where  $(k)^n$  represents an exponent calculation. It is the upper bound of  $\|\mathbf{d}\|_0$  because:

$$\|\mathbf{d}\|_0 \leq \|\mathbf{d}\|_1, \forall d_t \in \mathbb{N}, \forall t \in \mathbb{Z} \quad (11)$$

where

$$\|\mathbf{d}\|_0 = \|\mathbf{d}\|_1 \Leftrightarrow d_t \in \{0, 1\}, \forall t \in \mathbb{Z} \quad (12)$$

We assume that the (12) holds. By substituting this into the constraint of (9):

$$1 + (k-1) \sum_{n=1}^N r_n = (k)^N \quad (13)$$

This is a sum of geometric progression; one solution can be obtained as:

$$\mathbf{r}' = (1 \quad \dots \quad (k)^{n-1} \quad \dots \quad (k)^{N-1})^\top \quad (14)$$

It satisfies a uniformly covered receptive field:  $d_t^N(k, \mathbf{r}') = \begin{cases} 0 & t \notin \mathbb{S} \\ 1 & t \in \mathbb{S} \end{cases}$ , where  $\mathbb{S} := [-\frac{s^N-1}{2}, \frac{s^N-1}{2}] \cap \mathbb{Z}$  in 1D and the same in 2D, which satisfies the equivalent condition in (12) and thus is a solution to (9). Therefore, the atrous rate setting of  $(k)^{n-1}$  at the  $n^{\text{th}}$  atrous convolutional layer could lead to the largest and fully-covered receptive field under the condition that the same number of atrous convolutional layers is used.

## B. Atrous Convolutional Neural Network

We first introduce the ACNN structure briefly in these two paragraphs and then explain each component of the proposed ACNN in details in below sections.

With the proof in Sec. II-A, a receptive field of  $(k)^N$  could be achieved by a block of  $N$  atrous convolutional layers. Each node in the receptive field is linked evenly. In this paper, the kernel size of atrous convolutional layers is 3, following the settings used in [14]. A block of  $N$  atrous convolutional layers has a receptive field of  $(3)^N$ . We call this block as atrous block and the one specific with  $N$  atrous

convolutional layers as  $N$ -block, here  $N$  is expressed in the roman numeral.

The proposed ACNN is designed into multiple cascaded atrous blocks to increase the receptive field linearly by  $(3)^N$ . For achieving a  $H \times W$  (usually  $W = H$ ) whole-image coverage,  $H/(3)^N$  blocks are needed to be cascaded. For solving the gradient vanishing/exploding problems and facilitating back propagation, shortcut connections including residual learning, identity mapping and dense connection, and normalization methods including Batch Normalization (BN), Layer Normalization (LN), Instance Normalization (IN) and Group Normalization (GN), are explored and assessed.

1) *Atrous Block*: To determine the optimal ACNN structure, different atrous blocks are explored. As the test image size in this paper is 512 or 256, six atrous blocks (I-block, II-block, III-block, IV-block, V-block, VI-block) are assessed with the receptive field of 3, 9, 27, 81, 243, 729, respectively, as shown in Fig. 3. The feature channels of the input and output feature map are the same.

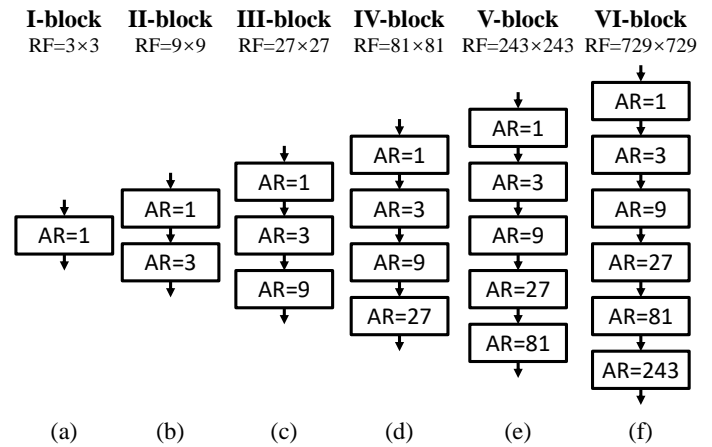


Fig. 3. Six atrous blocks: I-block, II-block, III-block, IV-block, V-block, VI-block with 1, 2, 3, 4, 5, 6 atrous convolutional layers inside the block. The Atrous Rate (AR) is set as  $(3)^{n-1}$  at the  $n^{\text{th}}$  layer,  $n \in [1, N] \cap \mathbb{N}$  is the sequence number of the atrous convolutional layer,  $N \in \{1, 2, 3, 4, 5, 6\}$  is the total number of atrous convolutional layers in each block.

The optimal atrous block is determined by experiments, as shown in Sec. III-A. Here, we state and use the conclusion in advance - atrous II-block is the optimal atrous block and is used in the following context.

2) *Shortcut Connection*: Plain DCNN experiences the degradation and gradient vanishing/exploding problems [15]. Shortcut connection is a solution to these problems. Three popular shortcut connections are explored in this paper: 1) residual learning [15], 2) identity mapping [16], 3) dense connection [17]. Dense connection is seen as a shortcut connection method, as it was proved to be re-exploring the feature maps while residual learning was proved to be re-using the feature maps in [18], hence it is classified as the same type of techniques as residual learning - shortcut connection in this paper. In residual learning, the normalization layer and ReLU are placed after the atrous convolutional layer and  $\mathbf{F}^{n-2}$  is added to  $\mathbf{F}^n$ . For identity mapping, the normalization layer and ReLU are placed before the atrous convolutional layer and  $\mathbf{F}^{n-2}$  is added to  $\mathbf{F}^n$ . In dense connection, the normalization layer and ReLU are placed before the atrous convolutional layer and  $\mathbf{F}^{n-1}$  is concatenated to  $\mathbf{F}^n$ . As the feature map is in high resolution and the layer number is large (64 layers for the RV and LV experiments while 128 layers for the aorta experiments) in this paper, fully dense connection could not be achieved due to the extremely high memory usage. In this paper, a dense connection is placed after 16 (for the RV and LV experiments)

or 32 (for the aorta experiments) atrous II-blocks, resulting in four dense connections in total. This grouped dense connection is called dense4 connection, as the atrous convolutional layers are concatenated four times.

The optimal shortcut connection is determined by experiments, as shown in Sec. III-B. Here we rely on the fact that residual learning is the optimal shortcut connection and is used in the following context.

**3) Normalization Method:** For DCNN, when the value distribution of shallow feature maps or parameters changes, the parameters of deep layers would be trained to fit this distribution change rather than to fit the real and useful content. This phenomenon was defined as interval covariate shift [19] and is detrimental to both the training speed and performance. Normalization is a popular method proposed for solving the interval covariate shift and gradient vanishing/exploding problems [19]. Firstly, the feature map  $F$  is divided into multiple groups. Based on different group division methods, the most four popular normalization methods for biomedical semantic image segmentation are:

BN [19] divides each channel as a group:

$$\mu = \frac{1}{B \times H \times W} \sum_{b=1}^B \sum_{h=1}^H \sum_{w=1}^W f_{b,h,w} \quad (15)$$

$$\delta^2 = \frac{1}{B \times H \times W} \sum_{b=1}^B \sum_{h=1}^H \sum_{w=1}^W (f_{b,h,w} - \mu)^2 \quad (16)$$

IN [20] divides each channel and each batch as a group:

$$\mu = \frac{1}{H \times W} \sum_{h=1}^H \sum_{w=1}^W f_{h,w} \quad (17)$$

$$\delta^2 = \frac{1}{H \times W} \sum_{h=1}^H \sum_{w=1}^W (f_{h,w} - \mu)^2 \quad (18)$$

LN [21] divides each batch as a group:

$$\mu = \frac{1}{H \times W \times C} \sum_{h=1}^H \sum_{w=1}^W \sum_{c=1}^C f_{h,w,c} \quad (19)$$

$$\delta^2 = \frac{1}{H \times W \times C} \sum_{h=1}^H \sum_{w=1}^W \sum_{c=1}^C (f_{h,w,c} - \mu)^2 \quad (20)$$

GN [22] divides each batch and multiple channels as a group:

$$\mu = \frac{1}{H \times W \times M} \sum_{h=1}^H \sum_{w=1}^W \sum_{m=(g-1) \cdot M+1}^{g \cdot M} f_{h,w,m} \quad (21)$$

$$\delta^2 = \frac{1}{H \times W \times M} \sum_{h=1}^H \sum_{w=1}^W \sum_{m=(g-1) \cdot M+1}^{g \cdot M} (f_{h,w,m} - \mu)^2 \quad (22)$$

Here,  $f$  is the element in each feature map group,  $B$  is the batch size,  $H$  is the feature map height,  $W$  is the feature map width,  $C$  is the feature channel number,  $M$  is the feature channel number in each group in GN,  $g$  is the feature group sequence in GN along the channel dimension. A systematic review and detailed group subdivision of these four normalization methods in biomedical semantic segmentation with U-Net structure could be found in [12].

In this paper, batch size of 1 is mainly explored, as it was proven that batch size of 1 out-performed larger batch sizes for biomedical semantic image segmentation [12]. For the proposed ACNN where the feature channel is the same for all intermediate feature maps, BN and IN are the same as Fine Group Normalization (FGN) (set

the group number of GN as the feature channel in this paper or the feature channel root in [12]) when the batch size is 1. Hence, FGN which also represents BN and IN, GN4 which sets the group number of GN as 4 and LN are explored for the subdivision of feature maps.

Then these grouped mean and variance are used to normalize the feature groups into a mean of 0.0 and a variance of 1.0:

$$\hat{f} = \frac{f - \mu}{\sqrt{\delta^2 + \epsilon}} \quad (23)$$

Here  $\epsilon$  is a small value to ensure the denominator of (23) is not zero. Finally, additional two parameters  $\gamma$  and  $\beta$  are applied to each feature channel to recover the representation ability of DCNN:

$$f'_{n,h,w} = \gamma \hat{f}_{n,h,w} + \beta \quad (24)$$

During inference, one way to apply BN, IN, LN and GN is to use the mean and variance of the current testing feature maps to normalize the testing feature maps. BN in this mode is called BN-train in this paper. There is an additional way to apply BN, i.e., to use the moving average mean and variance of the training feature maps to normalize the testing feature maps. BN in this mode is called BN-infer, which is also explored in this paper.

The optimal normalization method is selected based on experimental results, as shown in Sec. III-C. Here, we assume that - FGN is the optimal normalization method. FGN was also proven to be the optimal normalization method when using a U-Net structure for biomedical semantic image segmentation [12]. For a U-Net structure, FGN is different from BN and IN, as the feature channel changes inside the DCNN. To be consistent with [12] and for better generalizability, FGN is used as a representation of FGN, IN and BN in this paper.

**4) ACNN Architecture:** The final proposed ACNN architecture is shown in Fig. 4. Multiple atrous II-blocks with residual learning and FGN are cascaded. The number of residual II-blocks -  $(H-1)/8$  is determined by the input image size, i.e., 32 for a  $256 \times 256$  image while 64 for a  $512 \times 512$  image.

### C. Experimental Setup and Validation

Three cardiovascular MRI and CT datasets for RV, LV and aorta segmentation were used for validation of the proposed ACNN.

*a) Right Ventricle (RV):* 37 patients, with different levels of Hypertrophic Cardiomyopathy (HCM) were scanned with a 1.5T MRI scanner (Sonata, Siemens, Erlangen, Germany) [23], involving 6082 images with 10mm slice gap, 1.5 ~ 2mm pixel spacing, 19 ~ 25 times frames, and  $256 \times 256$  image size. Analyze (AnalyzeDirect, Inc, Overland Park, KS, USA) was used to label the ground truth. Rotation from  $-30^\circ$  to  $30^\circ$  with  $10^\circ$  as the interval was used to augment the images. Three groups, with 12, 12, and 13 patients respectively, were split randomly from the 37 patients for cross validations.

*b) Left Ventricle (LV):* 45 patients, from the SunnyBrook MRI data set [24] were used, it has 805 images with  $256 \times 256$  image size. Rotation from  $-60^\circ$  to  $60^\circ$  with  $2^\circ$  as the interval was used to augment the images. Three groups, with 15 patients respectively, were split randomly from the 45 patients for cross validations.

*c) Aorta:* 20 patients, from the VISCERAL data set [25], were used, 4631 CT images with  $512 \times 512$  image size. Rotation from  $-40^\circ$  to  $40^\circ$  with  $10^\circ$  as the interval was used to augment the images. Three groups, with 7, 7, and 6 patients respectively, were split randomly from the 20 patients for cross validations.

Image intensities were normalized to 0.0 ~ 1.0. Evaluation images were not split. For cross validations, two groups were used in the training stage while the other group was used in the testing stage. The kernel size of the last atrous convolutional layer is 1 while the kernel size of all the other atrous convolutional layers is 3. The momentum

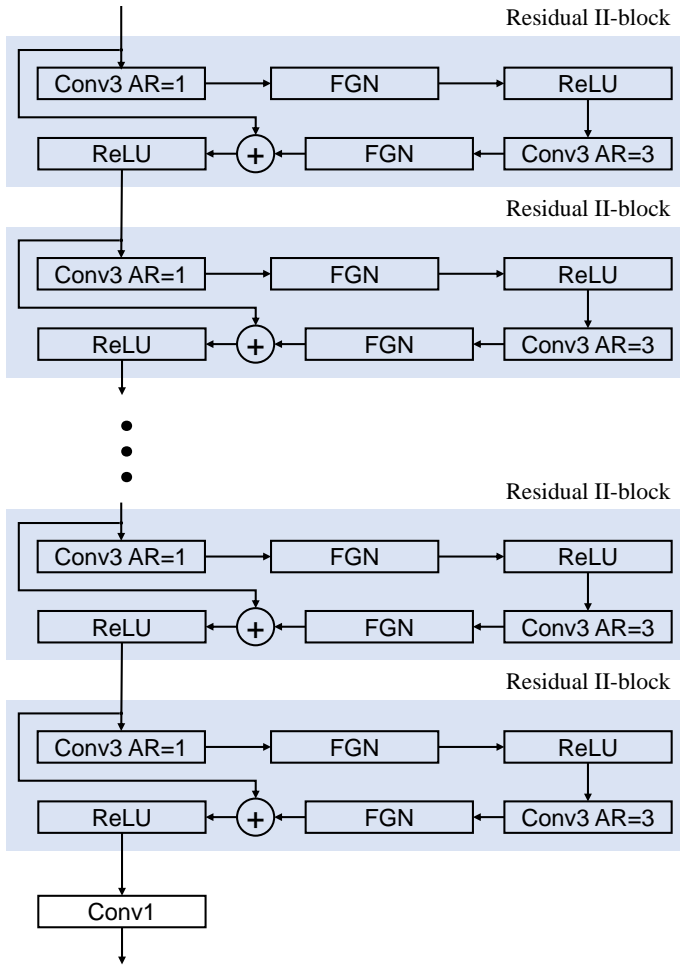


Fig. 4. The network architecture of the proposed ACNN. The number of residual II-blocks is determined by  $(H-1)/s$ ,  $H$  is the height or width of input image. AR - atrous rate, Conv3 - atrous convolution with kernel size of 3, Conv1 - atrous convolution with kernel size of 1.

was set as 0.9. Multiple epoch settings, i.e., 1, 2, or 3 and multiple learning rate schedules, i.e., dividing the learning rate by 5 or 10 at the second or third epoch, indicating an optimal learning schedule that: two epochs were trained and the learning rate was divided by 5 at the second epoch. Five initial learning rates: 1.5, 1.0, 0.5, 0.1, 0.05 were trained for each experiment and the highest accuracy was recorded as the final accuracy to avoid non-optimal hyper-parameter settings. For all experiments conducted, Stochastic Gradient Descent (SGD) was utilized as the optimizer.

Pixel-level softmax was applied after the proposed ACNN to transfer the network outputs into probabilities:

$$p_{nc} = \frac{e^{y_{nc}}}{\sum_{i=1}^{NC} e^{y_i}} \quad (25)$$

Here,  $y$  is the output of proposed ACNN,  $p$  is the predicted probability, NC is the number of predicted classes. Cross-entropy was used as the loss function:

$$Loss = - \sum_{i=1}^W \sum_{j=1}^H \sum_{nc=1}^{NC} L_{(i,j,nc)} \log(P_{(i,j,nc)}) \quad (26)$$

DSC was used to evaluate the segmentation accuracy:

$$DSC = 2 \cdot \frac{|L \cap P|}{|L| + |P|} \quad (27)$$

The DSC of the foreground is selected to represent the segmentation accuracy, as the DSC of the background is in the same trend as that of the foreground. The workers used were *Titan Xp* (12G memory) and *1080Ti* (11G memory) with the CPUs of an Intel® Xeon(R) CPU E5-1650 v4 @ 3.60GHz  $\times$  12 and an Intel® Xeon(R) CPU E5-1620 v4 @ 3.50GHz  $\times$  8.

The method was implemented with the Tensorflow Estimator Application Programming Interface (API). The atrous convolution and BN were programmed with *tf.layers*. The IN, LN and GN were programmed with *tf.contrib.layers*. The data was shuffled globally when generating the *tfrecords* file and was shuffled again with shuffle size of 500 when feeding images with *tf.data*, which ensures a random image input. The Tensorflow version used is 1.8.0. The process status of the CPU and GPU both influence the training speed. Training all models under exactly the same computer process status is not possible. For a fair speed comparison, the time recorded in this paper is for 100 iterations under the computer process status where all other processes are ended. The memory usage was recorded by using *watch nvidia-smi* command. The parameter amount is for the weights and biases in the atrous convolutional layers and was recorded based on *model.summary()* in Keras.

### III. RESULTS

Six atrous blocks were assessed and validated on the three datasets: RV, LV and aorta to select the optimal atrous block. For the RV and LV datasets with an image size of  $256 \times 256$ , 128 atrous I-blocks (Model 1), 32 atrous II-blocks (Model 2), 10 atrous III-blocks (Model 3), 3 atrous IV-blocks (Model 4), 1 atrous V-block (Model 5) were cascaded respectively for a whole-image receptive field. The feature channel was set as 12, 16, 24, 38, 64 to maintain a similar number of trainable parameters used in each model, this guaranteed a fair comparison between the five models. The parameter number in each model was  $1.66 \times 10^5$ ,  $1.46 \times 10^5$ ,  $1.51 \times 10^5$ ,  $1.44 \times 10^5$ , and  $1.48 \times 10^5$  respectively. For the aorta dataset with an image size of  $512 \times 512$ , 256 atrous I-blocks (Model 1), 64 atrous II-blocks (Model 2), 20 atrous III-blocks (Model 3), 6 atrous IV-blocks (Model 4), 2 atrous V-blocks (Model 5), and 1 atrous VI-block (Model 6) were cascaded respectively for a whole-image receptive field. The feature channel was set as 12, 16, 24, 38, 64, 80 respectively to maintain a similar number of trainable parameters used in each model. The parameter number was  $3.34 \times 10^5$ ,  $2.95 \times 10^5$ ,  $3.08 \times 10^5$ ,  $3.00 \times 10^5$ ,  $3.33 \times 10^5$ , and  $2.89 \times 10^5$  respectively. Before confirming the optimal shortcut connection and normalization method, identity mapping and FGN was used as the shortcut connection and normalization method respectively in this section of experiments. Detailed results are shown in Sec. III-A.

Three shortcut connections: residual learning, identity mapping and dense4 connection were explored and validated on the three datasets to select the optimal shortcut connection. Details are illustrated in Sec. III-B. Before confirming the optimal normalization method, FGN was used as the normalization method in this section of experiments. Four normalization methods: BN-infer, LN, FGN (the same as BN-train and IN in this paper), GN4 were validated on the three datasets to select the optimal normalization method and details are presented in Sec. III-C. Examples of the segmentation results are shown in Sec. III-D.

Three popular DCNNs were used for the comparison. (1) U-Net proposed in [11] with five max-pooling layers; (2) Optimized U-Net with FGN proposed in [12] with seven max-pooling layers to achieve the largest receptive field; and (3) a hybrid DCNN similar to the Deeplab proposed in [3] but with much less trainable parameters to decrease the memory usage, the intermediate eight blocks with

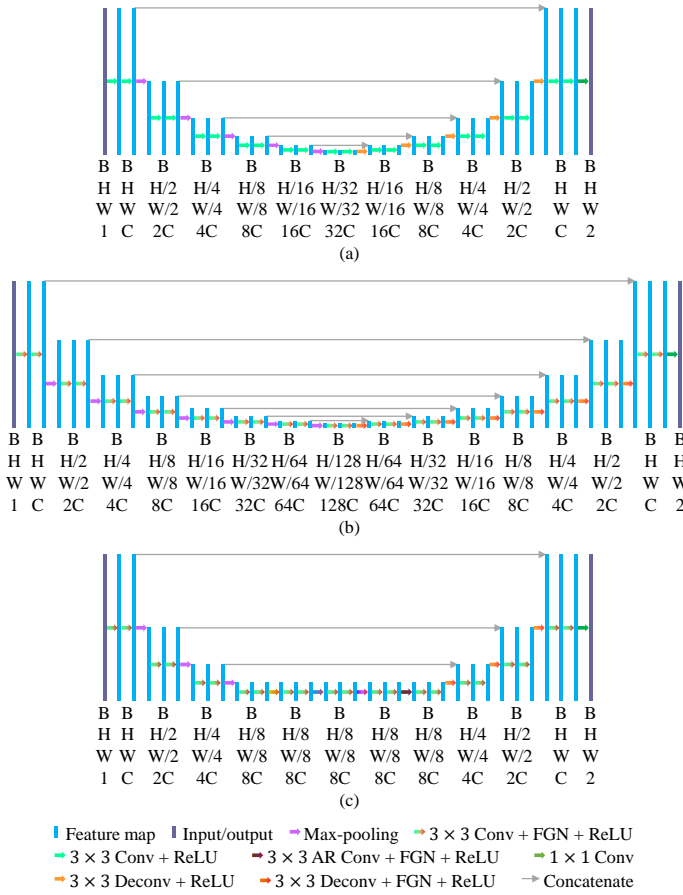


Fig. 5. The network architectures of three comparison DCNNs: (a) U-Net [11]; (b) optimized U-Net [12]; (c) hybrid network [3]; Conv - convolutional layers, Deconv - deconvolutional layers, AR Conv - atrous convolutional layers with atrous rate setting of (2, 4, 8, 16) respectively, FGN - fine grain normalization.

max-pooling and deconvolutional layers in the Optimized U-Net were replaced with four atrous convolutional blocks which were composed of two convolutional layers with atrous rates as 1 plus one atrous convolutional layer with atrous rate setting of (2, 4, 8, 16) respectively. The feature channel root was set as 16 for all methods. Details regarding the network structure are shown in Fig. 5. A detailed comparison regarding the accuracy, memory usage, and speed are given in Sec. III-E. It was known that slight difference exists even by training exactly with the same model setting in multiple times [26]. In this paper, this variance is given in Sec. III-F.

In the following paragraphs, RV-1 refers to the first cross validation (use the first group as the testing and use the second and third group as the training) of RV segmentation, this notation also applies to RV-2, RV-3, LV-1, LV-2, LV-3, Aorta-1, Aorta-2, and Aorta-3.

#### A. Atrous Block

The segmentation accuracy, optimal learning rate, memory usage and training time for 100 iterations of the five ACNN models for the RV segmentation, the five ACNN models for the LV segmentation, and the six ACNN models for the aorta segmentation are shown in Tab. I. We can see that for most of the experiments including RV-3, LV-1, LV-3, Aorta-1, Aorta-2 and Aorta-3, Model 2 with atrous II-blocks achieves the highest accuracy. For those experiments that Model 2 under-performs (including RV-1, RV-2, and LV-2), it still achieves reasonable accuracy. For the RV and LV experiments, Model 2 with atrous II-blocks also consumes the minimum amount of memory.

However, for the aorta experiments, this advantage no longer exists. This is because the aorta data is with a large image size of  $512 \times 512$ . This high resolution feature map propagation consumes a lot of memory and Model 2 contains many high resolution feature maps. The training time decreases along the number of atrous convolutional layers in each block - N for all the three datasets. The optimal learning rates show no major differences.

The mean DSC for each patient in the RV, LV and aorta dataset with using the five or six ACNN models as the segmentation methods are shown in Fig. 6. Model 2 with atrous II-blocks achieves the highest DSC for 12/37 RV patients, 18/45 LV patients and 8/20 aorta patients. For some patients, i.e., patient 31 in the RV dataset, patient 29 and 44 in the LV dataset, patient 10 and 15 in the aorta dataset show clearly that Model 2 with atrous II-blocks out-performs other ACNN models. The atrous II-block is concluded as the optimal atrous block and is used in all experiments below.

#### B. Shortcut Connection

The segmentation accuracy, optimal learning rate, memory usage and training time for 100 iterations of the atrous II-block ACNN for segmenting the RV, LV and aorta with different shortcut connections: residual learning, identity mapping and dense4 connection are shown in Tab. II. We can see that, even residual learning is not the shortcut connection which achieves the highest accuracy at most experiments. In fact, it achieves very similar accuracy to the highest value at those experiments where it under-performs, i.e., RV-3, LV-1, LV-2, LV-3, Aorta-1, and Aorta-2. Dense4 connection consumes the largest memory and takes the longest time to train. The consumed memory of the dense4 connection for the aorta experiment is an estimated value, as the real value is larger than 12G and the shown value is an optimized and approximate value. Residual learning takes almost a similar amount of memory and training time as identity mapping. The optimal learning rates show no major differences either.

The mean DSC for each patient in the RV, LV and aorta dataset with the three shortcut connections is shown in Fig. 7. For some patients, i.e. patient 6, 12, 31 in the RV dataset, patient 20 in the LV dataset, patient 19 in the aorta dataset, residual learning out-performs other shortcut connection methods. However, there are also some under-performed examples, i.e., patient 27 in the RV dataset, patient 29 in the LV dataset. Overall, residual learning is concluded as the optimal shortcut connection method and is used in later experiments.

#### C. Normalization Method

The mean DSC for each patient in the RV, LV and aorta dataset with the atrous II-block ACNN, residual learning and four normalization methods: BN-infer, LN, FGN, and GN4 is shown in Fig. 8. We can see that FGN (green color) achieves the highest accuracy at most patients. For some patients, i.e., patient 4, 14, 23 in the RV dataset, patient 39, 40 in the LV dataset, patient 17, 19 in the aorta dataset, FGN out-performs obviously. There isn't too much difference between the memory usage of the ACNNs with the four normalization methods (all around 1.65G for the RV and LV experiments and 9.64G for the aorta experiments). In terms of the training speed, FGN is similar to BN-infer and LN (around 10.0s for the RV and LV experiments while 60.0s for the aorta experiments), while GN4 is the slowest (around 14.5s for the RV and LV experiments while 95.5s for the aorta experiments). The optimal learning rates of BN-infer are usually very small and around 0.05 while this trend does not exist for the LN, FGN and GN4 method. FGN is selected as the optimal normalization method and is used in the following experiments.

TABLE I

THE MEAN $\pm$ STD DSC, OPTIMAL LEARNING RATE (OLR), MEMORY USAGE AND TRAINING TIME FOR 100 ITERATIONS FOR THE FIVE OR SIX ACNN MODELS WITH DIFFERENT ATROUS BLOCKS FOR THE RV, LV AND AORTA SEGMENTATION, HIGHEST DSCs ARE LABELLED IN BOLD AND RED.

Model	RV-1		RV-2		RV-3		Memory	Time
	mean $\pm$ std DSC	OLR	mean $\pm$ std DSC	OLR	mean $\pm$ std DSC	OLR		
Model 1	0.6588 $\pm$ 0.3333	0.5	<b>0.7253<math>\pm</math>0.2846</b>	1.5	0.6653 $\pm$ 0.3261	0.5	2.55G	14.5s
Model 2	0.6425 $\pm$ 0.3476	0.5	0.7169 $\pm$ 0.2812	0.5	<b>0.6825<math>\pm</math>0.3265</b>	0.5	1.65G	9.4s
Model 3	<b>0.6688<math>\pm</math>0.3284</b>	0.05	0.7167 $\pm$ 0.2831	0.05	0.6462 $\pm$ 0.3344	0.5	1.67G	6.3s
Model 4	0.6470 $\pm$ 0.3265	0.05	0.6685 $\pm$ 0.3174	0.05	0.6208 $\pm$ 0.3281	0.1	1.96G	4.6s
Model 5	0.6007 $\pm$ 0.3278	0.1	0.6442 $\pm$ 0.3205	0.05	0.5863 $\pm$ 0.3556	1.0	8.59G	3.5s
	LV-1		LV-2		LV-3			
Model 1	0.8807 $\pm$ 0.1831	1.5	0.8056 $\pm$ 0.2467	0.1	0.7909 $\pm$ 0.2451	1.5	2.55G	14.5s
Model 2	<b>0.9155<math>\pm</math>0.1107</b>	0.1	0.8590 $\pm$ 0.1627	1.0	<b>0.8186<math>\pm</math>0.2310</b>	0.5	1.65G	9.4s
Model 3	0.9118 $\pm$ 0.1172	0.5	<b>0.8721<math>\pm</math>0.1743</b>	0.05	0.8008 $\pm$ 0.2493	0.5	1.67G	6.3s
Model 4	0.8857 $\pm$ 0.1452	0.1	0.8580 $\pm$ 0.1513	1.5	0.7921 $\pm$ 0.2407	0.5	1.96G	4.6s
Model 5	0.8554 $\pm$ 0.1501	0.1	0.7844 $\pm$ 0.2204	0.05	0.7806 $\pm$ 0.2175	0.1	8.59G	3.5s
	Aorta-1		Aorta-2		Aorta-3			
Model 1	0.8255 $\pm$ 0.1833	0.1	0.7787 $\pm$ 0.2019	0.05	0.7973 $\pm$ 0.2185	1.5	11.72G	94.4s
Model 2	<b>0.8491<math>\pm</math>0.1543</b>	0.1	<b>0.7871<math>\pm</math>0.2095</b>	0.5	<b>0.8365<math>\pm</math>0.1726</b>	0.1	9.64G	62.5s
Model 3	0.8388 $\pm$ 0.1731	0.05	0.7575 $\pm$ 0.2528	0.5	0.8337 $\pm$ 0.1915	0.1	9.72G	43.1s
Model 4	0.8006 $\pm$ 0.1691	0.05	0.7235 $\pm$ 0.2794	0.05	0.7828 $\pm$ 0.2182	0.1	6.77G	31.8s
Model 5	0.7937 $\pm$ 0.1580	0.1	0.6998 $\pm$ 0.2619	0.5	0.7677 $\pm$ 0.2568	0.1	8.82G	22.2s
Model 6	0.7026 $\pm$ 0.2256	1.5	0.6564 $\pm$ 0.2629	0.5	0.7427 $\pm$ 0.2507	0.05	4.98G	24.1s

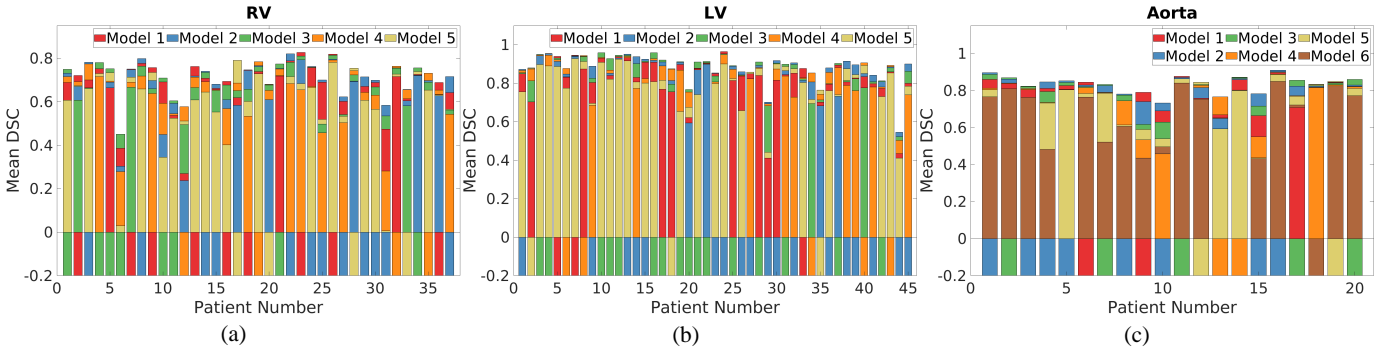


Fig. 6. The patient mean DSC for the RV (a), LV (b) and aorta (c) dataset with using different ACNN models: Model 1, Model 2, Model 3, Model 4, Model 5 and Model 6, the bars at the negative Mean DSC axis indicate the model that achieves the highest mean DSC for that patient while the bars at the positive Mean DSC axis show the mean DSCs achieved by different models.

TABLE II

THE MEAN $\pm$ STD DSC, OPTIMAL LEARNING RATE (OLR), MEMORY USAGE AND TRAINING TIME FOR 100 ITERATIONS FOR ATROUS II-BLOCK ACNNs WITH DIFFERENT SHORTCUT CONNECTIONS FOR THE RV, LV AND AORTA SEGMENTATION, HIGHEST DSCs ARE LABELLED IN BOLD AND RED.

Test	Residual learning				Identity mapping				Dense4 connection			
	mean $\pm$ std DSC	OLR	Memory	Time	mean $\pm$ std DSC	OLR	Memory	Time	mean $\pm$ std DSC	OLR	Memory	Time
RV-1	<b>0.6755<math>\pm</math>0.3226</b>	0.5			0.6425 $\pm$ 0.3476	0.5			0.6752 $\pm$ 0.3256	0.05		
RV-2	<b>0.7267<math>\pm</math>0.2839</b>	1.5	1.66G	9.8s	0.7169 $\pm$ 0.2812	0.5	1.65G	9.4s	0.7080 $\pm$ 0.2940	0.1	2.68G	10.5s
RV-3	0.6823 $\pm$ 0.3297	0.05			<b>0.6825<math>\pm</math>0.3265</b>	0.5			0.7080 $\pm$ 0.2940	0.1		
LV-1	0.9133 $\pm$ 0.1185	0.05			0.9155 $\pm$ 0.1107	0.1			<b>0.9190<math>\pm</math>0.0668</b>	0.05		
LV-2	0.8712 $\pm$ 0.1691	0.5	1.66G	9.8s	0.8590 $\pm$ 0.1627	1.0	1.65G	9.4s	<b>0.8726<math>\pm</math>0.1627</b>	0.5	2.68G	10.5s
LV-3	0.8153 $\pm$ 0.2346	0.5			<b>0.8186<math>\pm</math>0.2310</b>	0.5			0.8032 $\pm$ 0.2392	0.5		
Aorta-1	0.8449 $\pm$ 0.1457	0.5			<b>0.8491<math>\pm</math>0.1543</b>	0.1			0.8335 $\pm$ 0.1743	0.01		
Aorta-2	0.7820 $\pm$ 0.2318	0.1	9.65G	62.6s	<b>0.7871<math>\pm</math>0.2095</b>	0.5	9.64G	62.5s	0.7809 $\pm$ 0.2094	0.05	$\approx$ 11.89G	65.4s
Aorta-3	<b>0.8493<math>\pm</math>0.1554</b>	0.05			0.8365 $\pm$ 0.1726	0.1			0.8344 $\pm$ 0.1750	0.1		

#### D. Segmentation Details

Four examples of the RV, LV and aorta segmentation results are shown in Fig. 9. As the RV and LV dataset are not volumetric MRI images, hence only 2D segmentation slices are shown.

#### E. Comparison with Other Methods

The segmentation accuracy, optimal learning rate, and parameter number of the four different DCNNs: the proposed ACNN, hybrid network [3], optimized U-Net [12] and U-Net [11] on segmenting the RV, LV and aorta are shown in Tab. III. The optimized U-Net achieves the highest DSCs for 5 cross validations including RV-1,

LV-1, LV-2, LV-3, and Aorta-2, the proposed ACNN achieves the highest DSCs for 3 cross validations including RV-2, Aorta-1 and Aorta-3, the hybrid network achieves the highest DSC on 1 cross validation - RV-3. With achieving comparable DSCs to the other three methods, the proposed ACNN used much less trainable parameters. This advantage is largely due to the efficiency of full-scale feature maps inside the proposed ACNN. Compared to the out-performed DCNN - optimized U-Net, the proposed ACNN also consumes much less memory and training time for the RV and LV experiments (1.66G memory and 9.8s training time for 100 iterations for the proposed ACNN while 8.80G memory and 15.1s training time for 100 iterations

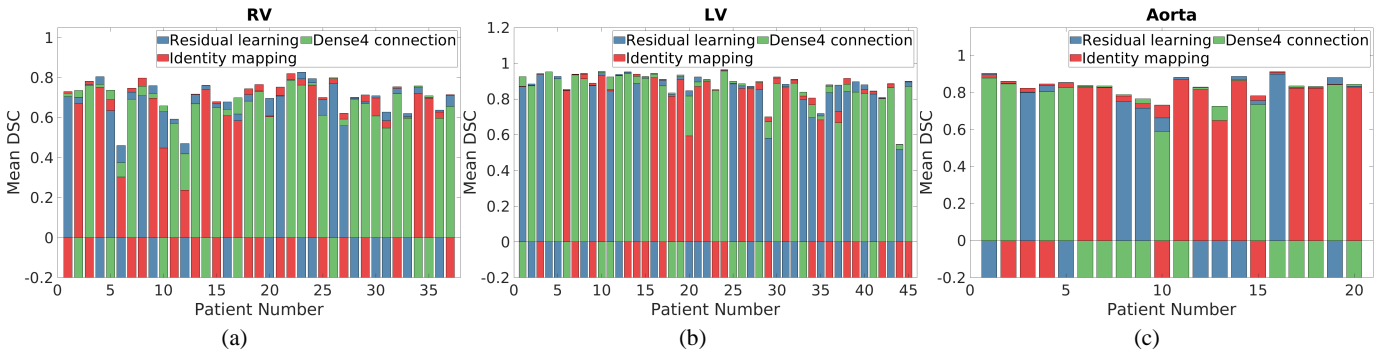


Fig. 7. The patient mean DSC for the RV (a), LV (b) and aorta (c) dataset with different shortcut connections: residual learning, identity mapping and dense4 connection, the bars at the negative Mean DSC axis indicate the shortcut connection that achieves the highest mean DSC for that patient while the bars at the positive Mean DSC axis show the mean DSCs achieved by different shortcut connections.

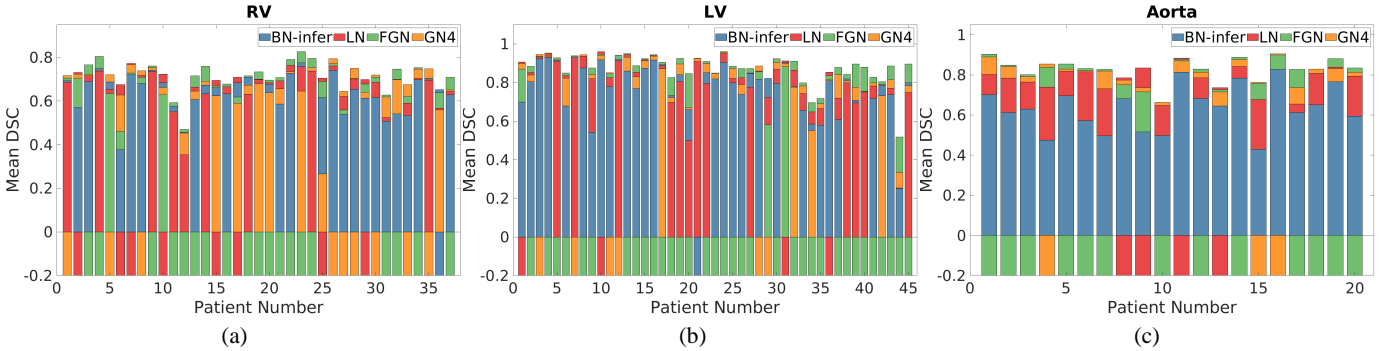


Fig. 8. The patient mean DSC for the RV (a), LV (b) and aorta (c) dataset with different normalization methods: BN-infer, LN, FGN and GN4, the bars at the negative Mean DSC axis indicate the normalization that achieves the highest mean DSC for that patient while the bars at the positive Mean DSC axis show the mean DSCs achieved by different normalization methods.

TABLE III

THE MEAN $\pm$ STD DSC, OPTIMAL LEARNING RATE (OLR), AND TRAINABLE PARAMETERS FOR THE FOUR DIFFERENT DCNNs FOR THE RV, LV AND AORTA SEGMENTATION, HIGHEST DSCs ARE LABELLED IN BOLD AND RED.

Test	The proposed ACNN		Hybrid network [3]		Optimized U-Net [12]		U-Net [11]	
	mean $\pm$ std DSC	OLR	mean $\pm$ std DSC	OLR	mean $\pm$ std DSC	OLR	mean $\pm$ std DSC	OLR
RV-1	0.6755 $\pm$ 0.3226	0.5	0.7101 $\pm$ 0.2875	1.0	<b>0.7204<math>\pm</math>0.2795</b>	0.5	0.6944 $\pm$ 0.2428	0.5
RV-2	<b>0.7267<math>\pm</math>0.2839</b>	1.5	0.7175 $\pm$ 0.2600	1.0	0.7002 $\pm$ 0.2900	0.05	0.6452 $\pm$ 0.3297	0.1
RV-3	0.6823 $\pm$ 0.3297	0.05	<b>0.6907<math>\pm</math>0.2862</b>	0.5	0.6636 $\pm$ 0.3047	0.1	0.6117 $\pm$ 0.3455	0.05
LV-1	0.9133 $\pm$ 0.1185	0.05	0.9205 $\pm$ 0.0995	1.0	<b>0.9241<math>\pm</math>0.0965</b>	0.05	0.9240 $\pm$ 0.0678	0.1
LV-2	0.8712 $\pm$ 0.1691	0.5	0.8930 $\pm$ 0.1300	0.5	<b>0.8932<math>\pm</math>0.1211</b>	0.05	0.8874 $\pm$ 0.1592	0.1
LV-3	0.8153 $\pm$ 0.2346	0.5	0.8306 $\pm$ 0.2030	0.1	<b>0.8434<math>\pm</math>0.1912</b>	1.5	0.8081 $\pm$ 0.2345	0.1
Aorta-1	<b>0.8449<math>\pm</math>0.1457</b>	0.5	0.8197 $\pm$ 0.2018	1.0	0.8302 $\pm$ 0.1652	0.5	0.8165 $\pm$ 0.1843	0.05
Aorta-2	0.7820 $\pm$ 0.2318	0.1	0.7846 $\pm$ 0.2145	1.5	<b>0.8102<math>\pm</math>0.1764</b>	0.5	0.7938 $\pm$ 0.2081	0.05
Aorta-3	<b>0.8493<math>\pm</math>0.1554</b>	0.05	0.7483 $\pm$ 0.3072	1.0	0.8419 $\pm$ 0.1737	1.0	0.7718 $\pm$ 0.2712	0.05
Parameters	1.46M(RV, LV) / 2.95M(Aorta)		23.1M		1384.2M		86.5M	

for the optimized U-Net). There are no obvious differences regarding the optimal learning rates.

The mean DSC for each patient in the RV, LV and aorta dataset with the four different DCNNs as the segmentation methods is shown in Fig. 10. We can see that U-Net (yellow color) under-performs obviously than the other three methods, especially for the RV and aorta data.

#### F. Multiple Runs

The proposed ACNN were trained additionally five times (plus the one in Tab. III, in total six times) for each cross validation. The mean and variance of six segmentation mean DSCs are shown in Tab. IV. We can see that the DSC variance is  $< 2\%$ , which is in the normal range -  $1\% \sim 2\%$  stated in [26] and is comparable to the DSC variance -  $0.97\% \sim 5.62\%$  when training U-Net in multiple

times [12]. The average DSCs in Tab. IV mostly are lower than the mean DSCs of the proposed ACNN in Tab. III. This is normal, as the mean DSCs in Tab. III were optimized by training five different initial learning rates. This optimization would not cause unfairness, as it was applied to all other experiments as well.

## IV. DISCUSSION

An atrous rate setting for determining the atrous rate at the  $n^{th}$  atrous convolutional layer as  $(k)^{n-1}$  where  $k$  is the convolutional kernel size is proposed. It can achieve the largest and fully-covered receptive field with a minimum number of atrous convolutional layers. Comparison experiments with traditional atrous rate settings, i.e., (1, 2, 4, 8, ...), (1, 2, 5, 9, ...) are not conducted due to: 1) smaller receptive field resulted by traditional atrous rate settings would not definitely indicate lower segmentation accuracy, as a large receptive field may



TABLE IV

THE MEAN AND VARIANCE OF THE SEGMENTATION MEAN DSC OF TRAINING THE SAME MODEL IN SIX TIMES, OLR - OPTIMAL LEARNING RATE.

Test	RV-1	RV-2	RV-3	LV-1	LV-2	LV-3	Aorta-1	Aorta-2	Aorta-3
Mean	0.6508	0.7045	0.6543	0.9117	0.8611	0.8069	0.8341	0.7830	0.8451
Variance	0.0187	0.0145	0.0171	0.0035	0.0191	0.0091	0.0156	0.0164	0.0083
OLR	0.5	1.5	0.05	0.05	0.5	0.5	0.5	0.1	0.05

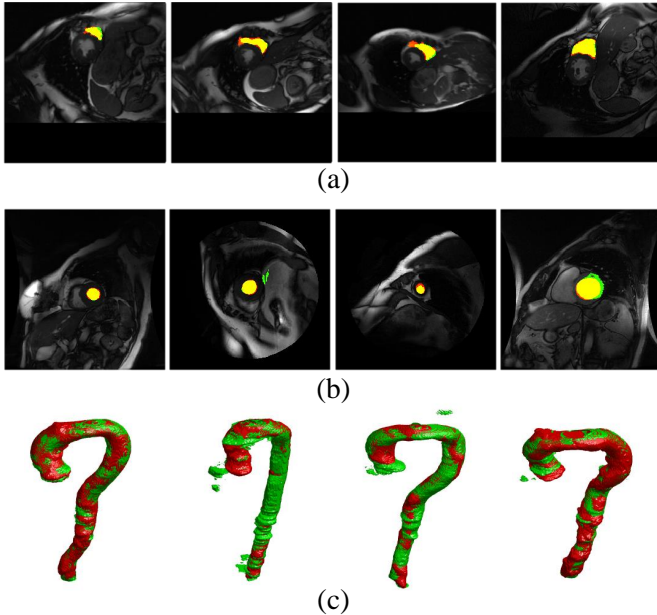


Fig. 9. Four examples of the RV (a), LV (b) and aorta (c) segmentation results. The red color indicates the ground truth, the green color indicates the prediction, hence the yellow color indicates the overlapped pixels which are correctly segmented.

be redundant when the target is small; 2) in addition to the receptive field, complex factors, i.e., the link number of each input node and the trainable parameters influence the segmentation accuracy too. The complex reasons behind a good segmentation make it difficult to judge the atrous rate setting from the segmentation accuracy. Hence, in this paper, detailed mathematical proof and derivation are given.

Six atrous blocks: I-block, II-block, III-block, IV-block, V-block, VI-block with a receptive field of 3, 9, 27, 81, 243, 729 respectively are proposed and assessed. For an atrous block with a larger receptive field, i.e., VI-block, a fewer number of blocks and a fewer total number of atrous convolutional layers are needed to cover the whole input image. Under the network framework in this paper, i.e., atrous block cascade, identity mapping, FGN, the experiments indicate that atrous II-block is optimal for biomedical semantic image segmentation. However, if the network framework is changed or the task is changed, the optimal atrous block may be different. For transferring the atrous blocks proposed in this paper to other works, additional exploration and assessment specific to the target task are essential to select the corresponding optimal atrous block.

Dense connection was proven to be efficient in [17]. In this paper, it is not adopted due to its similar segmentation accuracy and high memory consuming. Identity mapping was proven to be an improvement of residual learning in [16]. In this paper, it is not used due to its slightly lower robustness and stability. Finally, residual learning is used as the shortcut connection. BN, IN, LN and GN are the four most popular normalization methods used in biomedical semantic image segmentation. It was proven in [12] that FGN is the optimal normalization method for U-Net structure. In this paper, FGN

also out-performs other normalization methods and is used.

The proposed ACNN achieves comparable segmentation accuracy with the hybrid network, optimized U-Net and U-Net, but with using much less trainable parameters. We think this achievement comes from the efficient information contained in full-scale feature maps. This advantage is very useful when applying the trained model to mobile devices, as the trained model will require much less memory. For data with a smaller image size, i.e., the RV and LV dataset with image size  $256 \times 256$ , the proposed ACNN also consumes much less memory and training time. However, the consumed memory and training time increases significantly with the image size, i.e., the aorta dataset with image size  $512 \times 512$ . This would be further optimized with network architecture designs in our future work. Furthermore, target specific segmentation DCNNs are not compared in this paper, i.e., Omega-Net proposed for cardiac MRI segmentation [27] and Equally-weighted Focal U-Net proposed for class-imbalance stent graft marker segmentation [28], as additional target-specific algorithms related to the target character is usually applied in these methods and hence these methods usually may not be generalizable to other datasets.

Except Sec. III-F, all the other accuracy shown was recorded from the first training only. For a fair comparison, five initial learning rates are explored for each experiment to avoid setting the learning rate less optimally. This process may indicate an optimized accuracy, as a sub-optimized training would not out-perform among the five trainings. However, this process would not cause unfairness, as it is the same for all experiments.

The shown training time is only for 100 iterations and under a clear computer process status. This time could be much longer when the computer and GPU are filled with other processes. In practice, the whole training time takes up to 16 hours to train one model. As five learning rates were tested for each experiment, it took up to 4 days to show one DSC in above tables and figures. This training speed is based on `tf.layers` and `tf.contrib.layers` programming and may be different if the implementation is programmed differently. Hyper-parameters, i.e. the momentum and optimizer are selected based on experience. Different results may exist if different hyper-parameter settings are utilized.

Based on the author's knowledge, all codes were optimized as much as possible. Further optimization may exist and may influence the recorded memory usage and training time. The applications of the proposed ACNN are not limited to biomedical image segmentation, but also could be expanded to natural image segmentation and other pixel-level tasks, which needs further detailed validations.

## V. CONCLUSION

A new full-scale DCNN - ACNN is proposed with the use of cascaded atrous II-blocks, residual learning and FGN. A new atrous rate setting is proposed to achieve the largest and fully-covered receptive field with a minimum number of atrous convolutional layers. Six atrous blocks including I-block, II-block, III-block, IV-block, V-block, VI-block, three shortcut connections including residual learning, identity mapping, dense4 connection, and four normalization methods including BN, IN, LN, GN are assessed with detailed experiments to select the optimal method for the atrous block, shortcut connection and normalization layer. With much less trainable

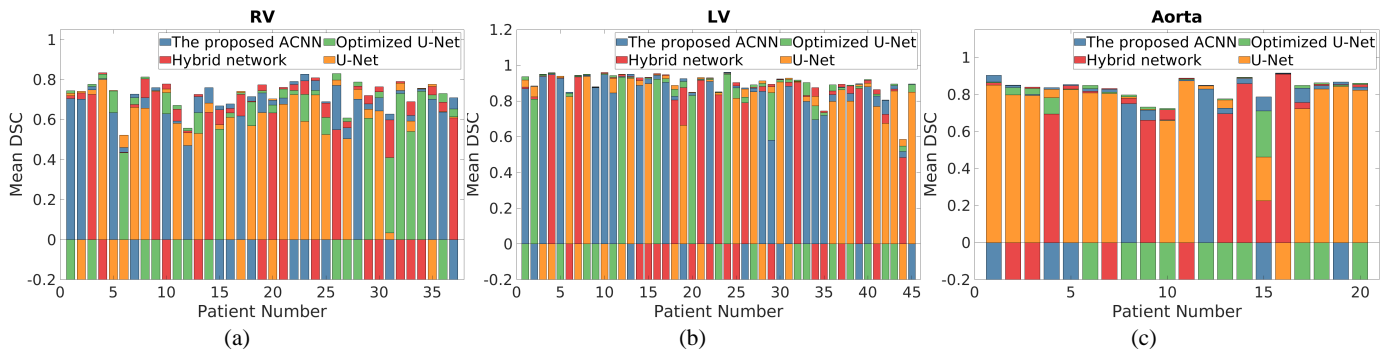


Fig. 10. The patient mean DSC for the RV (a), LV (b) and aorta (c) dataset with different DCNNs: the proposed ACNN, hybrid network [3], optimized U-Net [12] and U-Net [11], the bars at the negative Mean DSC axis indicate the DCNN that achieves the highest mean DSC for that patient while the bars at the positive Mean DSC axis show the mean DSCs achieved by different DCNNs.

parameters than that used in the hybrid network, optimized U-Net and U-Net, comparable accuracy is achieved by the proposed ACNN. The much less parameters needed in the proposed ACNN would contribute significantly to the community, as transferring DCNN methods onto mobile devices and realizing real-time performances are the two common challenges faced by the current DCNN methods. This paper contributes to some fundamental problems in DCNN with full-scale feature maps, i.e., the atrous rate setting, atrous block division, wider exploration and contribution from other researchers in the future would promote full-scale DCNNs greatly. Codes will be available online to show the detailed implementation.

## VI. ACKNOWLEDGEMENT

The authors thank Qing-Biao Li for the collection and processing of the data. We thank the support of NVIDIA Corporation with the donation of the Titan Xp GPU used for this research.

## REFERENCES

- [1] A. Krizhevsky, I. Sutskever, and G. E. Hinton, "Imagenet classification with deep convolutional neural networks," in *Advances in neural information processing systems*, 2012, pp. 1097–1105.
- [2] T.-Y. Lin, P. Goyal, R. Girshick, K. He, and P. Dollár, "Focal loss for dense object detection," in *Proceedings of the IEEE Conference on Computer Vision and Pattern Recognition*, 2017, pp. 2980–2988.
- [3] L.-C. Chen, G. Papandreou, I. Kokkinos, K. Murphy, and A. L. Yuille, "DeepLab: Semantic image segmentation with deep convolutional nets, atrous convolution, and fully connected crfs," *IEEE transactions on pattern analysis and machine intelligence*, vol. 40, no. 4, pp. 834–848, 2018.
- [4] Y. LeCun, Y. Bengio, and G. Hinton, "Deep learning," *Nature*, vol. 521, no. 7553, pp. 436–444, 2015.
- [5] J. Long, E. Shelhamer, and T. Darrell, "Fully convolutional networks for semantic segmentation," in *Proceedings of the IEEE conference on computer vision and pattern recognition*, 2015, pp. 3431–3440.
- [6] V. Badrinarayanan, A. Kendall, and R. Cipolla, "Segnet: A deep convolutional encoder-decoder architecture for image segmentation," *IEEE Transactions on Pattern Analysis & Machine Intelligence*, no. 12, pp. 2481–2495, 2017.
- [7] F. Yu and V. Koltun, "Multi-scale context aggregation by dilated convolutions," in *ICLR*, 2016.
- [8] P. Wang, P. Chen, Y. Yuan, D. Liu, Z. Huang, X. Hou, and G. Cottrell, "Understanding convolution for semantic segmentation," *arXiv preprint arXiv:1702.08502*, 2017.
- [9] L.-C. Chen, G. Papandreou, F. Schroff, and H. Adam, "Rethinking atrous convolution for semantic image segmentation," *arXiv preprint arXiv:1706.05587*, 2017.
- [10] T. Pohlen, A. Hermans, M. Mathias, and B. Leibe, "Full-resolution residual networks for semantic segmentation in street scenes," in *2017 IEEE Conference on Computer Vision and Pattern Recognition (CVPR)*. IEEE, 2017, pp. 3309–3318.
- [11] O. Ronneberger, P. Fischer, and T. Brox, "U-net: Convolutional networks for biomedical image segmentation," in *International Conference on Medical image computing and computer-assisted intervention*. Springer, 2015, pp. 234–241.
- [12] X.-Y. Zhou and G.-Z. Yang, "Normalization in training u-net for 2d biomedical semantic segmentation," *IEEE Robotics and Automation Letters*, 2019.
- [13] W. Luo, Y. Li, R. Urtasun, and R. Zemel, "Understanding the effective receptive field in deep convolutional neural networks," in *Advances in Neural Information Processing Systems*, 2016, pp. 4898–4906.
- [14] K. Simonyan and A. Zisserman, "Very deep convolutional networks for large-scale image recognition," *arXiv preprint arXiv:1409.1556*, 2014.
- [15] K. He, X. Zhang, S. Ren, and J. Sun, "Deep residual learning for image recognition," in *Proceedings of the IEEE conference on computer vision and pattern recognition*, 2016, pp. 770–778.
- [16] —, "Identity mappings in deep residual networks," in *European conference on computer vision*. Springer, 2016, pp. 630–645.
- [17] G. Huang, Z. Liu, K. Q. Weinberger, and L. van der Maaten, "Densely connected convolutional networks," in *Proceedings of the IEEE conference on computer vision and pattern recognition*, vol. 1, no. 2, 2017, p. 3.
- [18] Y. Chen, J. Li, H. Xiao, X. Jin, S. Yan, and J. Feng, "Dual path networks," in *Advances in Neural Information Processing Systems*, 2017, pp. 4467–4475.
- [19] S. Ioffe and C. Szegedy, "Batch normalization: Accelerating deep network training by reducing internal covariate shift," in *International Conference on Machine Learning*, 2015, pp. 448–456.
- [20] J. L. Ba, J. R. Kiros, and G. E. Hinton, "Layer normalization," *stat*, vol. 1050, p. 21, 2016.
- [21] D. Ulyanov, A. Vedaldi, and V. Lempitsky, "Instance normalization: The missing ingredient for fast stylization. corr (2016)," *arXiv preprint arXiv:1607.08022*, 2016.
- [22] Y. Wu and K. He, "Group normalization," *arXiv preprint arXiv:1803.08494*, 2018.
- [23] X.-Y. Zhou, G.-Z. Yang, and S.-L. Lee, "A real-time and registration-free framework for dynamic shape instantiation," *Medical image analysis*, vol. 44, pp. 86–97, 2018.
- [24] P. Radau, Y. Lu, K. Connelly, G. Paul, A. Dick, and G. Wright, "Evaluation framework for algorithms segmenting short axis cardiac mri," *The MIDAS Journal-Cardiac MR Left Ventricle Segmentation Challenge*, vol. 49, 2009.
- [25] O. Jimenez-del Toro, H. Müller, M. Krenn, K. Gruenberg, A. A. Taha, M. Winterstein, I. Eggel, A. Foncubierta-Rodríguez, O. Goksel, A. Jakab *et al.*, "Cloud-based evaluation of anatomical structure segmentation and landmark detection algorithms: Visceral anatomy benchmarks," *IEEE transactions on medical imaging*, vol. 35, no. 11, pp. 2459–2475, 2016.
- [26] V. Sze, Y.-H. Chen, T.-J. Yang, and J. S. Emer, "Efficient processing of deep neural networks: A tutorial and survey," *Proceedings of the IEEE*, vol. 105, no. 12, pp. 2295–2329, 2017.
- [27] D. M. Vigneault, W. Xie, C. Y. Ho, D. A. Bluemke, and J. A. Noble, " $\omega$ -net (omega-net): Fully automatic, multi-view cardiac mr detection, orientation, and segmentation with deep neural networks," *Medical image analysis*, vol. 48, pp. 95–106, 2018.
- [28] X.-Y. Zhou, C. Riga, S.-L. Lee, and G.-Z. Yang, "Towards automatic 3d shape instantiation for deployed stent grafts: 2d multiple-class and class-imbalance marker segmentation with equally-weighted focal u-net,"

in *2018 IEEE/RSJ International Conference on Intelligent Robots and Systems (IROS)*. IEEE, 2018, pp. 1261–1267.